1 **An alveolus lung-on-a-chip model of *Mycobacterium fortuitum* lung infection**

2 Victoria Ektnitphong[1], Beatriz R.S. Dias[1], Priscila C. Campos[1] and Michael U. Shiloh[1,2]

3 [1]Department of Internal Medicine and [2]Department of Microbiology

4 University of Texas Southwestern Medical Center

5 5323 Harry Hines Blvd., Y9.308

6 Dallas, TX 75390-9113

7 Corresponding author: Michael.shiloh@utsouthwestern.edu

ABSTRACT

Lung disease due to non-tuberculous mycobacteria (NTM) is rising in incidence. While both two dimensional cell culture and animal models exist for NTM infections, a major knowledge gap is the early responses of human alveolar and innate immune cells to NTM within the human alveolar microenvironment. Here we describe development of a humanized, three-dimensional, alveolus lung-on-a-chip (ALoC) model of *Mycobacterium fortuitum* lung infection that incorporates only primary human cells such as pulmonary vascular endothelial cells in a vascular channel, and type I and II alveolar cells and monocyte-derived macrophages in an alveolar channel along an air-liquid interface. *M. fortuitum* introduced into the alveolar channel primarily infected macrophages, with rare bacteria inside alveolar cells. Bulk-RNA sequencing of infected chips revealed marked upregulation of transcripts for cytokines, chemokines and secreted protease inhibitors (SERPINs). Our results demonstrate how a humanized ALoC system can identify critical early immune and epithelial responses to *M. fortuitum* infection. We envision potential application of the ALoC to other NTM and for studies of new antibiotics.

22 **INTRODUCTION**

23 Nontuberculous mycobacteria (NTM) represent a diverse group of environmental organisms
24 found in varied natural habitats such as soil, water, and vegetation (Mercaldo et al., 2023).
25 Traditionally considered opportunistic pathogens of people with structural or immune deficits, lung
26 disease secondary to NTM is increasing in incidence in women and people over 65 years of age
27 (Winthrop et al., 2020). Among the NTM, *M. fortuitum* is the second most frequently encountered
28 rapidly-growing NTM after *Mycobacterium abscessus*, and can cause a spectrum of infections
29 including pulmonary, skin and soft tissue, and disseminated infections (Roquet-Baneres et al.,
30 2023, Kim et al., 2023). NTM lung infections are more frequent and more severe in
31 immunocompromised individuals and individuals with pre-existing conditions such as
32 bronchiectasis, severe chronic obstructive pulmonary disease (COPD), cystic fibrosis, organ
33 transplant and cancer (Roquet-Baneres et al., 2023, Kim et al., 2023). Treatment of NTM lung
34 disease can be complex due to the presence of antibiotic resistance, medication side effects and
35 extended duration of drug treatment. More efforts are needed to develop new, safe and efficacious
36 therapeutics and to shorten treatment duration (Johansen and Kremer, 2020, Orme and Ordway,
37 2014, Kremer, 2020). In addition, the rising incidence of NTM lung infections among individuals
38 without defined predisposing conditions indicates that a greater understanding of the immune
39 response to NTM lung infection is needed.

40 Expanding the scope of knowledge of the dynamic interactions between humans and NTM is
41 essential for developing effective prevention and treatment strategies for NTM lung disease, but
42 gaining such knowledge has been hindered by the lack of suitable *in vitro* and *in vivo* models of
43 NTM lung infection (Baldwin et al., 2019). Current *in vitro* models typically use traditional two-
44 dimensional cell culture methods with primary human $CD14^+$ peripheral blood-derived
45 macrophages or immortalized monocytic cell lines THP-1 and U937 (Kilinc et al., 2022), and
46 alveolar epithelial cell lines such as A549 (Rampacci et al., 2020). Although immortalized cell lines

allow for large-scale screening and assay reproducibility, a major disadvantage is that they may not completely replicate myeloid cell responses in humans, especially in the unique alveolar microenvironment. For example, the use of PMA to differentiate THP-1 and U937 cells into adherent macrophage-like cells alters monocytic surface markers, transcriptional activities, and cytokine production (Rampacci et al., 2020). One recent advance beyond traditional two-dimensional systems has been adaptation of primary human airway-derived organoids to the study of *M. tuberculosis* and *M. abscessus* pathogenesis and drug susceptibility (Alcaraz et al., 2022, Iakobachvili et al., 2022, Leon-Icaza et al., 2023, Kim et al., 2024). Animal models have also been established to study host immune responses to NTM and for testing potential antimicrobial compounds and vaccines. Most animal models of NTM lung infection use mice as the host species including for *M. abscessus* (Caverly et al., 2015, De Groote et al., 2014) and *Mycobacterium avium* (Gonzalez-Perez et al., 2013, Gangadharam, 1995). However, the variable virulence of NTM in model organisms makes establishing consistent animal models challenging. For example, *M. avium* can establish a productive lung infection in immunocompetent mice, whereas *M. abscessus* is typically rapidly cleared and requires immunocompromised mice to achieve a similar outcome (Chan et al., 2016). Animal models for other NTM species such as *M. fortuitum* are lacking, delaying progress towards understanding shared and unique molecular mechanisms of pathogenicity for various NTM. Thus, developing *in vitro* models that can recapitulate the human lung microenvironment using primary human cells has the potential to advance the study of pulmonary NTM infections, and is a critical step towards developing improved prevention, vaccine and treatment strategies.

The alveolus lung-on-a-chip (ALoC) is an innovative microfluid device composed of microfabricated channels and chambers that mimic the architecture and cellular composition of the lung alveolus, the initial site of interaction for pulmonary NTM infection (Bethencourt et al., 2024). The “chip” contains two overlapping channels, parallel to each other, that are separated by

72 a porous membrane. It features alveolar epithelial cells lining one channel and pulmonary
73 microvascular endothelial cells (HMVECs) lining the other to closely replicate the alveolar-
74 capillary interface of the human lung (Jain et al., 2018). Because the cell types grow in distinct
75 channels, media or air flow through the channels can be independently controlled to create distinct
76 environments for the cells. Additional advantages of the ALoC include the ability to generate an
77 air-liquid interphase (ALI) that is hallmark of the alveolus and application of mechanical stretch
78 that is essential for the proper differentiation of alveolar epithelial cells into type I (AT1) and type
79 II (AT2) pneumocytes. In that respect, the ALoC helps overcome one of the major obstacles of *in*
80 *vitro* studies of alveolar epithelial cells, namely, simultaneously differentiating both AT1 and AT2
81 cells in culture by leveraging stretch and growth factor addition (Li et al., 2018). Thus, compared
82 to traditional tissue culture methods, the ALoC system provides a physiologically relevant
83 environment to study cells and pathogens of the human lung and has been applied to several
84 pathogens including *E. coli* (Huh et al., 2010), *M. tuberculosis* (Thacker et al., 2020), *Aspergillus*
85 *fumigatus* (Hoang et al., 2022), *Staphylococcus aureus* (Bai et al., 2022, Deinhardt-Emmer et al.,
86 2020), and influenza virus (Bai et al., 2022, Deinhardt-Emmer et al., 2020).

87 The complex interaction between *M. fortuitum* and the human alveolar epithelial and immune cells
88 remains poorly understood. Here, we develop and use a fully humanized ALoC model as a
89 platform to study the host-pathogen interactions of *M. fortuitum* within the alveolar
90 microenvironment. By recapitulating key features of the alveolar interface, including cellular
91 composition, mechanical forces, and biochemical gradients, this model offers a unique
92 opportunity to investigate the dynamics of *M. fortuitum* infection in a controlled and reproducible
93 manner. Through integration of advanced imaging techniques and transcriptomic analyses, we
94 identify macrophages as the primary cell type infected in the alveolus and upregulation of several
95 inflammatory pathways after *M. fortuitum* infection of the humanized ALoC. We propose
96 application of the humanized alveolus lung-on-a-chip as a new model to study NTM infections.

RESULTS

Two types of lung chips have been developed to date, one that approximates a bronchial airway (Benam et al., 2015, Benam et al., 2016) and another more like an alveolus (**Figure 1A**) (Huh et al., 2012a, Huh et al., 2010, Huh et al., 2012b). Since early NTM infection occurs in the alveolus, we chose the alveolus lung-on-a-chip (ALoC) as our working model for NTM infection (**Figure 1B**), as previously demonstrated with *E. coli* (Huh et al., 2010) and *M. tuberculosis* (Mishra et al., 2023, Thacker et al., 2020). We initially decided to use *M. fortuitum* to model airway NTM infection using the ALoC model both because it is rapidly-growing, with a doubling time of 2-3 hours (Qin et al., 1999), and because amongst the rapid growers it has one of the highest age-adjusted incidence of disease (Donohue, 2021).

Constructing a functional ALoC requires meticulously following a stepwise protocol (**Supplemental Figure 1A**). Briefly, the membranes of individual chips are chemically activated, coated with extracellular matrix and then human alveolar epithelial cells are added to the air (or apical) channel. After three days, human primary lung microvascular endothelial cells are introduced to the vascular (or basal) channel. Once cells are confluent (~1 day), the alveolus-on-a-chip is connected to regulated media flow (30 uL/hr) in both channels. The next day, the apical channel media is removed, generating an air-liquid interface (ALI), and after 2 days of ALI, stretch is introduced to mimic breathing (5% stretch intensity, 0.2 Hz) and induce surfactant production (Thacker et al., 2020). After two days of stretch we add differentiated human $CD14^+$ peripheral blood-derived macrophages (hereafter called 'macrophages') from anonymous donors to the top channel. To assess the donor compatibility of the alveolar epithelial cells and macrophages in the apical channel, we used immunofluorescence to compare AT1 and AT2 cell differentiation, cell morphology and distribution of cells along the apical channel of ALoCs with and without macrophages. In ALoCs without macrophages, a monolayer of both AT1 and AT2 cells was distributed equally across the apical channel (**Figure 1C, Supplemental Figure 1B**). High

122 resolution images of ALoCs without macrophages highlighted distinct AT1 and AT2 cell types after
123 15 days in culture on the ALoC (**Figure 1D**). Three-dimensional reconstruction of the ALoC
124 demonstrated the more cuboidal morphology of AT2 cells and the flatter morphology of AT1 cells
125 (**Figure 1D, far right**). Cross sectional imaging of the airway channel further highlighted the nuclei
126 in the basal region of the apical channel with interspersed AT1 and AT2 cells (**Figure 1E**). While
127 the majority of cells were either AT1 or AT2 cells, a small number of KRT5 positive basal like cells
128 were also observed in the airway channel (**Supplemental Figure 1C**). Finally, in the vascular
129 channel, we observed a confluent monolayer of endothelial cells lining the entirety of the channel
130 via staining for VE-Cadherin, a marker of endothelial cells (**Supplemental Figure 1D**).

131 We next turned to our analysis of ALoCs with macrophages (**Figure 2A**). In ALoCs with
132 macrophages, the monolayer of differentiated AT1 and AT2 cells appears intact and unaltered by
133 the addition of macrophages 24 hours prior (**Figure 2B, 2C, Supplemental Figure 1E**).
134 Macrophages were observed residing above of the alveolar epithelial monolayer (**Figure 2D**).
135 Although we introduced the same number of macrophages as alveolar epithelial cells, we
136 observed many fewer macrophages overall, suggesting that the majority of added macrophages
137 did not adhere tightly to the epithelial layer and were washed away (**Supplemental Figure 1F**).
138 To address this question, we quantified the number of macrophages residing on three ALoCs and
139 compared it to the number of macrophages seeded. We found that approximately 2.1×10^3 total
140 macrophages or 7% of the number seeded were present on the ALoCs at the end of the
141 experiment. Stitched images of ALoCs containing macrophages also showed that, despite the
142 loss of introduced macrophages, adherent macrophages were sufficient to evenly distribute
143 across the entire apical channel (**Figure 2B; Supplemental Figure 1E**). Despite the addition of
144 macrophages, AT cell distribution was comparable to uninfected ALoCs without macrophages
145 (**Figure 1D; Figure 2C).** From these experimental observations, namely that AT1 and AT2 cell
146 differentiation was maintained after the addition of primary human $CD14^+$ peripheral blood

147 macrophages, we concluded that macrophages could safely be added to the human ALoC model
148 without dramatically altering epithelial biology.

149 After establishing the ALoC model with human macrophages, we next incorporated mCherry-
150 expressing *M. fortuitum* to the system. We introduced mCherry-expressing *M. fortuitum* at an
151 estimated multiplicity of infection (MOI) of ~1 for the approximate number of AT1 and AT2 cells on
152 the chip (~3.0 x 10^4) (**Figure 3A**). We plated serial dilutions of the inoculum and determined the
153 concentration of *M. fortuitum* added to the ALoCs was approximately 3.15x10^4 CFU/mL. When
154 ALoCs were infected with *M. fortuitum* in the absence of macrophages, we observed large clumps
155 of bacteria scattered across the ALoC (**Figure 3B, 3C**). Along the apical channel in *M. fortuitum*-
156 infected ALoC, we also observed areas that lacked strong immunofluorescence signal that we did
157 not observe in uninfected ALoCs with or without macrophages (**Figure 3B, image center**). Higher
158 resolution imaging analysis suggested loss of viability of AT1 and AT2 cells and a more rounded
159 cell morphology, particularly for AT2 cells (**Figure 3C**). HT1 staining was also more diffuse in *M.*
160 *fortuitum*-infected ALoCs. In addition, while ~17% of cells were double positive for HT1 and HT2
161 staining in uninfected ALoCs (**Figure 3D, 3E**), we observed a significant increase in cells that
162 stained with both HT1 and HT2 antibodies in *M. fortuitum*-infected ALoCs without macrophages
163 (**Figure 3F, 3G)**. Though we observed large clumps of bacteria, *M. fortuitum* cord-like structures
164 were not observed within the initial 24 hours of infection. Taken together, introducing *M. fortuitum*
165 to the ALoC model at an approximate MOI of 1 generated a productive infection with sustained
166 growth of bacteria and epithelial cell responses consistent with active infection.

167 We next wanted to determine how *M. fortuitum* grows on ALoC in the presence of human
168 macrophages (**Figure 4A**). Twenty-four hours after seeding, ALoCs previously seeded with
169 macrophages were infected with *M. fortuitum* as described above. Notably, the alveolar epithelial
170 and pulmonary microvascular endothelial cells lining the chips were from the same donors as for
171 ALoCs without macrophages. On ALoCs with macrophages infected with *M. fortuitum*, there was

172 suitable distribution of AT2 cells across the chips (comparable to infected ALoCs without
173 macrophages). In contrast to *M. fortuitum*-infected ALoC without macrophages, we observed that
174 most bacteria were found to be intracellular within macrophages with significantly fewer bacterial
175 clumps (**Figure 4B-D**) and cord-like structures were not observed. Cross-sectional and three-
176 dimensional analysis of the ALoC with macrophages highlighted that *M. fortuitum* were residing
177 within macrophages (**Figure 4D**). To quantify bacteria within either AT1 or CD14+ cells, we
178 analyzed 10 z-stacks from 3 independent ALoCs containing macrophages. We used three-
179 dimensional reconstructions and ortho-projections to assign bacteria within AT1 cells (HT1+) or
180 macrophages ($CD14^+$) and found that bacteria were found more often in macrophages than AT1
181 cells (**Figures 4B, 4E)** To quantify bacteria within either AT2 cells (HT2+) or macrophages
182 ($CD14^+$), we performed a similar analysis with 3 ALoCs containing macrophages and determined
183 that bacteria were found more often in macrophages than AT2 cells (**Figures 4C, 4F**). Of note,
184 due to technical limitations of fluorophores we could use, quantifying bacteria within AT1 cells,
185 AT2 cells, and macrophages simultaneously could not be done within the same AloC. Taken
186 together, we conclude that in the presence of macrophages overlying alveolar epithelial cells, *M.*
187 *fortuitum* are ingested by macrophages, preventing extracellular growth and bacterial clumping.
188 Such an infection may also prevent loss of epithelial cell integrity.

189 To assess the response of human ALoC to *M. fortuitum* infection, we used bulk RNA sequencing
190 to compare the transcriptional status of *M. fortuitum* infected ALoC with macrophages to
191 uninfected ALoC with macrophages. After infection at an MOI of 1 for 24 hours, we collected total
192 RNA from the apical channel containing AT1 cells, AT2 cells and macrophages for sequencing.
193 While there was some heterogeneity in the response, as would be expected in a primary infection,
194 we observed 1454 genes were more than 2-fold upregulated, while 588 were more than 2-fold
195 downregulated (**Figure 5A, B**). Amongst the upregulated genes, we observed significant
196 upregulation of key cytokines such as tumor necrosis factor (*TNF*), granulocyte-macrophage

197 colony-stimulating factor (*GM-CSF* or *CSF2*), macrophage colony-stimulating factor (*M-CSF* or
198 *CSF3*), interleukin 1A (*IL1A*), interleukin 1B (*IL1B*), interleukin 6 (*IL6*), and interleukin 8 (*IL8*),
199 along with the alarmin, calprotectin (*S100A8* and *S100A9*) (**Figure 5C**). We also observed several
200 chemokines upregulated including the chemokine (C-X-C motif) ligand family members *CXCL1,*
201 *CXCL2, CXCL3, CXCL5, CXCL6, CXCL10* and *CXCL11* and the C-C motif chemokine ligand
202 family members *CCL2, CCL5, CCL20* and *CCL28* (**Figure 5C**). Finally, we also noted that many
203 secreted serine protease inhibitor (SERPIN) genes were also upregulated by *M. fortuitum*
204 infection (**Figure 5D**). Using pathway analysis (Ge et al., 2018), we found that the most
205 significantly upregulated processes were involved in host defense including "response to
206 bacterium", "defense response to bacterium", "antimicrobial humoral response", "response to
207 molecule of bacterial origin" and "response to lipopolysaccharide" (**Table 1**). Likewise,
208 upregulated molecular functions included several annotated as involved in "signaling" in addition
209 to "cytokine" and various channel functions (**Table 2**). Taken together, our data highlight the acute
210 inflammatory response of humanized ALoC containing human macrophages to *M. fortuitum*
211 infection.

212 **DISCUSSION**

213 We report the development of a fully humanized ALoC model for alveolar NTM infection. This
214 model develops features consistent with initial primary alveolar infection, including infection of
215 both airway macrophages and occasional alveolar cells. Moreover, bulk RNA sequencing reveals
216 activation of an acute inflammatory signaling cascade, including induction of cytokines,
217 chemokines and alarmins like serpins and calprotectin, with potential roles in recruitment of
218 myeloid and lymphoid cells from the vasculature and in triggering a robust immune response to
219 restrict bacterial growth. These findings highlight the value of using the humanized lung on a chip
220 to model a primarily human infectious disease.

221 Prior studies using the alveolus-on-a-chip have included infection models, such as infection with
222 *E. coli* (Huh et al., 2010), *M. tuberculosis* (Thacker et al., 2020), *Aspergillus fumigatus* (Hoang et
223 al., 2022), *Staphylococcus aureus* (Bai et al., 2022, Deinhardt-Emmer et al., 2020), and influenza
224 virus (Bai et al., 2022, Deinhardt-Emmer et al., 2020). The alveolus-on-a-chip has also been used
225 to determine the effect of mechanical strain on inflammation and particle uptake (Huh et al., 2010),
226 pulmonary thrombosis (Jain et al., 2018), and mechanotransduction and pulmonary edema (Li et
227 al., 2019). In the context of *M. tuberculosis* and *A. fumigatus* infection models, addition of human
228 monocytes/macrophages impacts pathogenesis (Thacker et al., 2020, Hoang et al., 2022). With
229 *M. tuberculosis*, cord-like structures are observed compressing macrophage nuclei (Mishra et al.,
230 2023). We did not observe a similar phenomenon with *M. fortuitum* infection of human
231 macrophages on the ALoC, which might be due to differences in the cell walls of the organisms
232 or other factors that impact the growth characteristics of *M. tuberculosis* (slow) as compared to
233 *M. fortuitum* (rapid). Alternatively, differences in the time after infection used for analysis (24 hours
234 in this study versus 72 hours (Mishra et al., 2023)) or imaging techniques may also account for
235 these differences. In a different model system using human bronchial epithelial cells, some
236 mycobacteria formed surface biofilms that ultimately caused apical non-apoptotic cell death
237 (Barclay et al., 2024). Because our infection model was limited to 24 hours, we did not observe
238 biofilm formation, but we did note some loss of cell viability and monolayer disruption, consistent
239 with the observations made with other mycobacterial species (Barclay et al., 2024).

240 We identified a transcriptional signature of early human alveolar infection with *M. fortuitum*. Some
241 notable findings include marked upregulation of important cytokines and chemokines that may be
242 involved in stimulating an early innate immune response to airway infection. For example, both
243 IL6 and IL8 are key cytokines involved in neutrophil recruitment to the airway (Fu and Harrison,
244 2021), and such recruited cells could have both beneficial (contributing to NTM killing) and
245 detrimental (involvement in tissue damage and bronchiectasis) effects (Alkarni et al., 2023).

246 While there have been previous studies of human peripheral blood transcriptional responses in
247 the context of pulmonary NTM infection (Wang et al., 2024, Cowman et al., 2018, Lindestam
248 Arlehamn et al., 2022) or tuberculosis (Tabone et al., 2021, Berry et al., 2010), as well as efforts
249 to determine transcriptional responses in human lung tissue from tuberculosis patients (Wang et
250 al., 2023a), to our knowledge this is the first analysis of the early interaction of an NTM with a
251 humanized ALoC. Interestingly, in the RNA sequencing analysis of PBMCs from individuals
252 infected with *M. avium*, TNF signaling was enriched, and individual genes such as those for
253 *SERPINA1* and calprotectin were modestly upregulated (Lindestam Arlehamn et al., 2022).
254 Calprotectin was also upregulated by *M. avium* infection in an air-liquid interface model of primary
255 human bronchial epithelial cells (Barclay et al., 2023). Likewise, in a proteomics analysis of serum
256 exosomes in humans with NTM infection, a variety of serpins including SERPINA1 and
257 SERPINA5 were enriched in patients with *M. abscessus* or *M. avium* infection (Wang et al.,
258 2023b). Recent work has found the induction of cytosolic SERPINs may protect *M. marinum*
259 infected macrophages from cathepsin B mediated lysosomal rupture and cell death (Nobs et al.,
260 2024), a process called lysoptosis that is evolutionary conserved from *C. elegans* to mammals
261 (Luke et al., 2022). Thus, SERPIN induction by *M. fortuitum* infection, potentially within infected
262 macrophages, may act to protect infected cells from lysoptosis. Of note, because we used bulk
263 RNA sequencing, we were unable to identify the precise cellular source of transcriptional changes
264 identified in our analysis. Future single cell sequencing studies will be necessary to determine the
265 responses of individual cell types within the model system, and how such responses impact
266 intercellular communication. Taken together, our bulk RNAseq analysis has identified unique
267 features of early alveolar NTM infection.

268 There are several limitations to our model. First, because our model uses all primary human cells,
269 genetic manipulation of the various cellular constituents is impractical, though primary human
270 monocytes can be transduced with lentivirus to abrogate gene expression (Campbell and Spector,

271 2012, Franco et al., 2017). Alternatively, use of genetically modified human or mouse cell lines
272 can overcome this limitation, though immortalized cell lines have their own inherent drawbacks.
273 Second, because primary cells, whether pulmonary epithelial cells, pulmonary vascular cells or
274 PBMCs, are obtained from unique individuals, genetic variation generates greater complexity.
275 Third, to optimize infection and cognizant that not all bacteria would adhere to the alveolar channel
276 or be ingested by macrophages or AT1/AT2 cells, we chose to use an MOI of 1, which is not likely
277 to be reflective of the number of bacteria that reach the terminal alveoli during a natural infection.
278 Future work will compare a range of MOI with the ALoC system and other NTM. Finally, though
279 our model does allow multiple cell types (epithelia, endothelia and myeloid cells) to interact with
280 each other and the NTM in the alveolar microenvironment, the interactions are limited to the cells
281 added to the chamber, and thus do not include all the possible myeloid and lymphoid cells that
282 could be recruited to the airway in the setting of pulmonary mycobacterial disease, such as
283 neutrophils (Kimmey et al., 2015), eosinophils (Bohrer et al., 2021) or innate lymphoid cells
284 (Ardain et al., 2019).

285 In conclusion, we have developed a fully humanized alveolus on a chip model of pulmonary NTM
286 infection. By capturing the complexity of NTM in three dimensions and with multiple cell types, as
287 would be found in a human lung, this model creates an opportunity to better characterize the
288 cellular and molecular mechanisms that mediate the outcome of human airway NTM infections.
289 Because NTM infections are on the rise, particularly in individuals with cystic fibrosis,
290 bronchiectasis and people with HIV, it may be useful to apply this technology to determine the
291 relative impact of genetic risk alleles (i.e. for those with cystic fibrosis) or coinfection with HIV on
292 the alveolar transcriptional responses or bacterial survival in the alveolus over time. Furthermore,
293 by leveraging this system to directly compare responses to other common human pulmonary NTM
294 infections, such as *M. avium* (Cristancho-Rojas et al., 2023, Varley and Winthrop, 2022, Donohue,
295 2021), *M. kansasii* and *M. abscessus* (Toure et al., 2023, Lagune et al., 2023, Cristancho-Rojas

296 et al., 2023, Ordway et al., 2008, Klever et al., 2023) future studies could identify shared and
297 unique survival strategies used by each organism, and establish distinct immune pathways
298 responsive to each pathogen which could function to limit or exacerbate infection, or be used
299 clinically as biomarkers of disease. Finally, as new drugs are developed to treat pulmonary NTM
300 infection, we envision applying this model for the simultaneous assessment of efficacy (i.e.
301 reduction in bacterial load) and cellular toxicity via infusion of test compounds into the vascular
302 channel.

303 **Materials and Methods**

304 **Bacteria**

305 *Mycobacterium fortuitum* subsp. *fortuitum* strain was obtained from ATCC (strain TMC 1529). We
306 transformed *M. fortuitum* with a vector containing *mCherry* driven by the GroEL constitutive
307 promoter.

308 **Primary Cell Culture**

309 Primary human alveolar epithelial cells (ATs) were obtained from Cell Biologics (H-6053). Prior to
310 seeding on Alveolus Lung-on-Chips (ALoCs), ATs were expanded *in vitro* in a T25 flask coated
311 with a 1% gelatin-based coating solution (Cell Biologics, catalog #6950) and complete medium
312 comprising of base media and supplements (Lonza, CC-3118). Medium was prepared according
313 to manufacturer's instructions using all supplements except GA-1000 where 1% Pen-Strep
314 solution (Gibco 15140-122) was added instead along with 5% FBS and hereby called Small
315 Airway Growth Medium (SAGM). Primary human microvascular endothelial cells were purchased
316 from Lonza (CC-2527). Human Lung Microvascular Endothelial cells (HMVECs) were expanded
317 in a T75 in complete medium comprising of base media and supplements (Lonza, CC-3202).
318 Medium was prepared according to manufacturer's instructions using all supplements except GA-
319 1000 where 1% Pen-Strep solution was used instead along with 5% FBS and hereby called EGM-

320 2MV. Both primary cell lines were cultured at 37°C in 5% CO_2 until ~80% confluency before
321 detachment with TrypLE Express (Gibco 12604013) and use on the ALoC.

322 One week prior to seeding the macrophages on the ALoC, peripheral blood mononuclear cells
323 (PBMCs) were obtained from buffy coats from anonymous donors (Carter BloodCare). PBMCs
324 were isolated using Ficoll (Cytivia, 17144003) and SepMate50 tubes from StemCell Technologies
325 (85450). $CD14^+$ monocytes were positively selected from the PBMCs using CD14 Microbeads
326 (Miltenyi, 130-050-201) and seeded onto uncoated petri dishes. The monocytes were cultured
327 overnight in RPMI medium (Gibco 11875-093) supplemented with 10% heat-inactivated human
328 serum obtained from the buffy coat of the donor, 1% HEPES buffered solution (Lonza CC-5022),
329 1% sodium pyruvate (Gibco 11360-070), and 50 ng/mL human granulocyte-macrophage colony-
330 stimulating factor (GM-CSF) (Peprotech 300-03-100UG) and is hereby called macrophage
331 medium. The next day, the serum in the medium was changed to 10% FBS for the remainder of
332 the culturing. $CD14^+$ monocytes were differentiated to human monocyte-derived macrophages
333 (HMDMs) for 7 days at 37°C in 5% CO_2 until use on the ALoCs. GM-CSF was added to the
334 macrophage medium for the first 4 days to differentiate the $CD14^+$ monocytes.

335 **Human Alveolus LoC Model**

336 ALoCs fabricated with polydimethylsiloxane (PDMS) were purchased from Emulate. The chips
337 were activated using a 0.5 mg/mL solution comprised of ER-1 and ER-2 (Emulate) that was
338 protected from light during the activation process. Working in a dark biosafety cabinet, both the
339 top and bottom channel were filled completely with ER-1/ER-2 and placed under a UV light for 10
340 min, inspected for bubbles with a brightfield microscope and placed under the UV light for an
341 additional 10 min. After activation of all chips, the top and bottom channels were coated with an
342 extracellular matrix (ECM) solution specific to the cell type. The top channel (ATs) was coated with
343 an ECM solution containing Collagen IV at 200 µg/mL (Sigma C5533), Fibronectin at 30 µg/mL
344 (Millipore Sigma F2006) and Laminin at 5µg/mL (Sigma L6274). The bottom channel (endothelial

345 cells) was coated with an ECM solution containing Collagen IV at 200 µg/mL and Fibronectin at
346 30 µg/mL. All ECM components and solutions were kept on ice and prepared by manufacturer's
347 recommendations. With an empty 200 µL pipette tip plugged into each outlet port, 100 uL of ECM
348 solution were added to the respective channels by expelling ECM solution from pipette tip and
349 plugging the inlet ports with the tip. The ECM-coated ALoCs were incubated at 4°C overnight and
350 the next day each channel was washed twice with 200 µL of respective medium. Respective
351 mediums were left in each channel prior to cell seeding and ALoCs were stored at 4°C until cell
352 seeding.

353 ATs were seeded first in the top channel of all ALoCs. After detaching the cells from the T75 flasks,
354 they were adjusted to a concentration of 1 x 10^6 cells/mL in SAGM medium described above. The
355 bottom channels were filled with SAGM medium during epithelial cell seeding. 50 µL of the AT cell
356 suspension was pipetted into the top channel rapidly and checked under a microscope to ensure
357 correct seeding density and cell homogeneity. Of note, the top channel volume is ~28 µL total,
358 but to ensure no bubbles are introduced, the channels are overfilled and the flow-through gently
359 aspirated. Once all chips were seeded, they were placed in a chip cradle (Emulate) and incubated
360 at 37°C for at least 2 hours. After confirming all cells had attached, each top and bottom channel
361 were gently washed with 200 µL of warm SAGM medium and incubated overnight at 37°C.
362 HMVECs were seeded 2-3 days later in the bottom channels of all ALoCs. Prior to HMVEC cell
363 seeding, media was replenished daily for the ATs seeded on the ALoCs. The SAGM medium used
364 for maintenance of the ATs on the chips (hereby called AT Maintenance Medium) was
365 supplemented with Dexamethasone at 100 nM (Sigma D4902), Keratinocyte growth factor (KGF)
366 at 5 ng/mL (Thermo Fisher PHG0094), 8-Br-cAMP at 50 µM (Sigma B7880), and Isobutyl
367 methylxanthine (IBMX) at 25 µM (Sigma I7018). When HMVECs reached ~80% confluency, they
368 were detached and adjusted to a concentration of 5 x 10^6 cells/mL in EGM-2MV medium
369 (described above). The bottom channels of all ALoCs were filled with EGM-2MV medium prior to

370 seeding. 20 µL of the HMVEC cell suspension was pipetted rapidly into the bottom channel and
371 checked under the microscope for correct seeding density and cell homogeneity. The bottom
372 channel volume is ~6 µL total. Similarly to the top channel, the bottom channel was overfilled to
373 prevent the introduction of bubbles to the channel. The chip was then immediately flipped upside
374 down and placed in the chip cradle to ensure cells were seeded on the porous membrane in the
375 bottom channel. Once all ALoCs were seeded and flipped upside down, they were incubated at
376 37°C for at least 2 hours until all cells were attached. After all cells had attached, the bottom
377 channel was washed with 200 µL of warm EGM-2MV medium and incubated overnight at 37°C.

378 Prior to attaching ALoCs to Pods, warm EGM-2MV and AT Maintenance medium were degassed
379 using a Steriflip device for 5 min each to prevent air bubbles being trapped in the microfluidic lines
380 of the Pod. 3 mL of each medium were pipetted into its respective reservoir within the Pod. Using
381 Emulate's Zoe, the Pods were primed with medium to prevent bubbles from impeding medium
382 flow to the ALoCs. Once primed, each ALoC was snapped into each respective Pod. To further
383 help prevent bubble formation within the microfluidic lines, a Regulate Cycle was performed on
384 each chip via the Zoe. The ALoCs from this point on were harbored within the Pods and fresh
385 medium was exchanged through the chip at a flow rate of 30 µL/hr supplied by the Zoe.

386 After 24 hours of continuous media flow on all ALoCs, air-liquid interface (ALI) was introduced to
387 all ALoCs by removing all medium from the top channel and changing the top channel from liquid
388 media flow to air. The bottom channel medium was changed to ALI medium which comprised of
389 a Medium 199 base (Thermo Fisher 11043023) supplemented with 10 ng/mL Human Epidermal
390 Growth Factor (Peprotech AF-100-15), 3 ng/mL Human Basic Fibroblast Growth Factor
391 (Peprotech AF-100-18B), 0.125 ng/mL Human Vascular Endothelial Growth Factor (Peprotech
392 AF-100-20), 1 µg/mL Hydrocortisone (Sigma H0135), 10 µg/mL Heparin (Sigma H3149), 80 µM
393 di-butyryl cAMP (Sigma B7880), 1mM L-Glutamax (Gibco 35050-061), 20 nM Dexamethasone
394 (Sigma D4902), 1% Pen-Srep solution (Gibco 125140-122), and 2% FBS. Bottom channel liquid

395 flow rate was set to 30 µL/hr and fresh ALI medium was replenished in the bottom channel
396 reservoir every 2-3 days. After 48 hours of ALI, mechanical stretch (5%, 0.20 Hz) was initiated
397 using the Zoe. All ALoCs were maintained in this way until seeding of macrophages and infection
398 with *M. fortuitum*.

399 **Macrophage Seeding on ALoCs**

400 After 7 days of differentiation with M-CSF to HMDMs, macrophages were detached from petri
401 dishes using ice-cold 5 mM EDTA in PBS and gentle scraping. HMDMs were centrifuged at 300xg
402 for 5 min and resuspended in a 1:1 ratio of AT Maintenance Medium (without dexamethasone)
403 and Macrophage Medium to a concentration of 1 x 10^6 cells/mL. ALoCs were removed from the
404 Zoe and detached from the Pods, and top channel was washed with 200 µL of HPAEC
405 Maintenance Medium. With medium still in the top channel, 50 µL of HMDM cell suspension was
406 rapidly pipetted through the top channel. ALoCs were placed in square petri dishes and incubated
407 at 37°C with 5% CO_2 for 3-4 hours to allow attachment to the top channel. Once attached, ALoCs
408 were attached back to Pods after priming and after 2 hours of a Regulate Cycle were returned to
409 ALI.

410 ***M. fortuitum* Infection on Human ALoC**

411 Upon returning ALoCs to ALI conditions after macrophage attachment to the ALoCs, ALI medium
412 was replaced with ALI medium without penicillin/streptomycin, to avoid impacting subsequent
413 bacterial infection. Twenty-four hours after returning to ALI conditions, the ALoCs were infected
414 with *M. fortuitum*. mCherry-expressing *M. fortuitum* was cultured at 37°C in liquid 7H9 medium
415 (BD Difco 271310) supplemented with 10% OADC enrichment (BD 212351), 50 µg/mL
416 Kanamycin (Sigma 60615) and 0.05% Tyloxapol (Sigma T8761) until it reached an OD_{600} 0.5 –
417 0.7. The culture was pelleted by centrifugation at 3500 RPM for 10 min. The pellet was washed
418 three times with 50 mL of 1X PBS (-Ca^+/-Mg^+) by centrifugation at 3500 RPM for 10 min, and

419 resuspended in 5 mL PBS for a slow spin to remove cell debris at 500 RPM for 5 min. The
420 supernatant was collected and passed through a 26-gauge needle three times to generate a
421 single-cell suspension. The bacterial suspension was adjusted to an MOI of 1 with respect to the
422 epithelial cells in HPAEC Maintenance Medium, and 50 µL of the *M. fortuitum* suspension was
423 pipetted rapidly through the top channel. The ALoCs were incubated at 37°C for 1 hr. under static
424 conditions, and then washed three times with epithelial medium before returning ALoCs back to
425 Pods and into the Zoe for another Regulate Cycle. ALI was initiated again and the ALoCs were
426 infected for a total of 24 hours.

427 **RNA Extraction from ALoCs**

428 ALoCs were removed from the Zoe and Pods. Top and bottom channels were washed three times
429 with 200 µL of ice-cold 1X DPBS (-Ca^+/-Mg^+). An empty p200 filtered tip was inserted into the
430 bottom inlet, bottom outlet, and top outlet ports. 200 µL of TRIzol reagent (Invitrogen #15596026)
431 was pipetted in each ALoC by rapidly pressing and releasing the plunger three times before
432 collecting the supernatant in an RNase-free 1.5 mL tube. This process was repeated once more
433 for a total of ~400 µL of supernatant. TRIzol was added to each tube of RNA to a final volume of
434 1 mL. The RNA was stored at -80°C before extraction using the Qiagen RNeasy Mini Columns
435 (74106). AT and macrophage lysates were thawed on ice and incubated at room temperature for
436 5 min. 200 µL of chloroform per 1 mL of lysates was added to each tube, shaken vigorously for
437 15 sec., incubated at room temperature for 2-3 min, and centrifuged for 5 min at 12,000xg at 4°C.
438 The aqueous phase was transferred to fresh RNase-free tubes and the rest of the RNA extraction
439 was performed according to the Qiagen RNeasy Mini Column Kit. Extracted RNA was stored at -
440 80°C until use for library preparation and RNA-sequencing.

441 **Library Preparation and RNA-sequencing**

442 Samples were analyzed on an Agilent Tapestation 4200 to determine level of degradation to
443 ensure that only high quality RNA was used (RIN Score 8 or higher). We used a Qubit 4.0
444 Fluorimeter (ThermoFisher) to determine RNA concentration prior to starting library prep. One
445 microgram of total DNAse treated RNA was then prepared with the TruSeq Stranded mRNA
446 Library Prep Kit (Illumina). Poly-A RNA was purified and fragmented before strand-specific cDNA
447 synthesis. cDNA was then A-tailed and indexed adapters ligated. After adapter ligation, samples
448 were PCR amplified and purified with AmpureXP beads, then validated again on the Agilent
449 Tapestation 4200. Before being normalized and pooled, samples were quantified by Qubit then
450 sequenced on the Illumina NextSeq 2000 using a P2-100 flowcell.

451 **Bulk RNA-sequencing Analysis**

452 All RNA-sequencing analyses were performed using integrated Differential Expression and
453 Pathways Analysis, iDEP 2.01 (Ge et al., 2018). Genes expressed at extremely low levels were
454 filtered out of the gene set by removing any genes with less than 0.4 counts per million (CPM) in
455 at least one sample (n=1) (**Supplemental Figure 3A**). 13,934 filtered genes were converted to
456 Ensembl gene IDs, normalized in edgeR and transformed via rlog. Hierarchical clustering of the
457 samples and the top 2000 genes were performed (**Supplemental Figure 3B**). We then performed
458 principal component analysis (PCA) using the 2000 most variable genes. Using DESeq2 and the
459 Wald test (FDR cutoff = 0.1, minimum fold change = 1.5), we generated adjusted p-values and
460 $\log_2$ fold changes. Gene expression was then compared between the “infected” AloCs and
461 “control_uninfected” ALoCs. A total of 1,454 genes were found to be downregulated ($\log_2$ fold
462 change <1) and 588 genes were upregulated ($\log_2$ fold change >1). Using analysis of variance
463 (ANOVA) and post-hoc pairwise t-tests, we evaluated between-group differences for each cluster
464 using these scaled expression values. We performed functional enrichment analysis using the
465 hypergeometric test in hypeR for enriched pathways within the differentially expressed gene set.
466 Enrichment analysis was run using significantly upregulated and significantly downregulated

467 genes. Gene categories with fewer than 15 genes were excluded. Gene categories were
468 considered significant if they had Benjamini-Hochberg adjusted *p*-values less than 0.1.

469 **Immunofluorescence**

470 ALoCs were washed three times with 200 µL of 1X DPBS and 200 uL of 4% PFA in PBS were
471 added to each channel of each ALoC for 20 min. at room temperature. ALoCs were then washed
472 three times with 200 µL of 1X DPBS and incubated for 30 min. at room temperature with 200 µL
473 of 0.1% Triton X-100 and 2% saponin. ALoCs were then washed three times with 200 µL of 1X
474 DPBS and incubated overnight at 4°C with primary antibody (1:100) (**Supplemental Table 1**).
475 ALoCs were washed again three times with 200 µL of DPBS and incubated with secondary
476 antibody (1:1000) (**Supplemental Table 1**) for 2 hours at room temperature, protected from light.
477 ALoCs were washed three times with 200 µL of 1X DPBS and incubated with DAPI for 10 min at
478 room temperature. They were washed again three times with 200 µL of 1X DPBS and stored at
479 4°C with both channels filled with 1X DPBS. Confocal images were acquired on a Nikon CSU W1
480 spinning disk confocal microscope with an CFI S Plan Fluor ELWD 20x objective and a laser
481 scanning confocal microscope Zeiss LSM 980 with an EC Plan-Neofluar 10x objective.

482 **Statistical analyses**

483 All statistical analyses were performed using GraphPad Prism Software (version 9). For *in vitro*
484 studies, data was analyzed using unpaired two-tailed *t*-test. For RNA sequencing analysis,
485 analysis of variance (ANOVA) and post-hoc pairwise t-tests were used to evaluate between-group
486 differences for each cluster using scaled expression values.

487 **ACKNOWLEDGEMENTS**

488 The authors thank Gautam Mahajan and Ben Swenor from Emulate Inc. for providing protocols
489 and support. The authors also thank core facilities at UT Southwestern Medical Center for their
490 important contributions to this work including the UT Southwestern McDermott Center Next

Generation Sequencing (NGS) Core and the Quantitative Light Microscopy Core, particularly the core director Marcel Mettlen, a Shared Resource of the Harold C. Simmons Cancer Center, supported in part by an NCI Cancer Center Support Grant, 1P30 CA142543-01 and Laura Alto of the UT Southwestern Microbiology Department Live Cell Imaging Facility, supported in part by an NIH S10 Instrumentation Award (1S10 OD034383).

COMPETING INTERESTS

All authors declare that they have no competing interests.

FUNDING

This work was supported by the National Institutes of Health U19 AI142784 to M.U.S.

DATA AVAILABILITY

Bulk RNA sequencing data has been deposited at the NCBI GEO database, GSE276053, and will be made publicly available at the time of publication.

AUTHOR CONTRIBUTIONS

Conceptualization, V.E., M.U.S.; Formal analysis, V.E., M.U.S.; Funding acquisition, M.U.S.; Investigation, V.E., B.R., P.C.; Project administration, M.U.S.; Supervision, M.U.S.; Visualization, M.U.S.; Writing – original draft, V.E., M.U.S.; Writing – review and editing, All authors.

References

ALCARAZ, M., ROQUET-BANERES, F., LEON-ICAZA, S. A., ABENDROTH, J., BOUDEHEN, Y. M., COUGOULE, C., EDWARDS, T. E. & KREMER, L. 2022. Efficacy and Mode of Action of a Direct Inhibitor of Mycobacterium abscessus InhA. *ACS Infect Dis,* 8**,** 2171-2186.

ALKARNI, M., LIPMAN, M. & LOWE, D. M. 2023. The roles of neutrophils in non-tuberculous mycobacterial pulmonary disease. *Ann Clin Microbiol Antimicrob,* 22**,** 14.

ARDAIN, A., DOMINGO-GONZALEZ, R., DAS, S., KAZER, S. W., HOWARD, N. C., SINGH, A., AHMED, M., NHAMOYEBONDE, S., RANGEL-MORENO, J., OGONGO, P., LU, L.,

515 RAMSURAN, D., DE LA LUZ GARCIA-HERNANDEZ, M., T, K. U., DARBY, M., PARK, E.,
516 KARIM, F., MELOCCHI, L., MADANSEIN, R., DULLABH, K. J., DUNLAP, M., MARIN-
517 AGUDELO, N., EBIHARA, T., NDUNG'U, T., KAUSHAL, D., PYM, A. S., KOLLS, J. K.,
518 STEYN, A., ZUNIGA, J., HORSNELL, W., YOKOYAMA, W. M., SHALEK, A. K.,
519 KLOVERPRIS, H. N., COLONNA, M., LESLIE, A. & KHADER, S. A. 2019. Group 3 innate
520 lymphoid cells mediate early protective immunity against tuberculosis. *Nature,* 570**,** 528-532.

521 BAI, H., SI, L., JIANG, A., BELGUR, C., ZHAI, Y., PLEBANI, R., OH, C. Y., RODAS, M., PATIL,
522 A., NURANI, A., GILPIN, S. E., POWERS, R. K., GOYAL, G., PRANTIL-BAUN, R. &
523 INGBER, D. E. 2022. Mechanical control of innate immune responses against viral infection
524 revealed in a human lung alveolus chip. *Nat Commun,* 13**,** 1928.

525 BALDWIN, S. L., LARSEN, S. E., ORDWAY, D., CASSELL, G. & COLER, R. N. 2019. The
526 complexities and challenges of preventing and treating nontuberculous mycobacterial
527 diseases. *PLoS Negl Trop Dis,* 13**,** e0007083.

528 BARCLAY, A. M., NINABER, D. K., LIMPENS, R., WALBURG, K. V., BARCENA, M.,
529 HIEMSTRA, P. S., OTTENHOFF, T. H. M., VAN DER DOES, A. M. & JOOSTEN, S. A. 2024.
530 Mycobacteria develop biofilms on airway epithelial cells and promote mucosal barrier
531 disruption. *iScience,* 27**,** 111063.

532 BARCLAY, A. M., NINABER, D. K., VAN VEEN, S., HIEMSTRA, P. S., OTTENHOFF, T. H. M.,
533 VAN DER DOES, A. M. & JOOSTEN, S. A. 2023. Airway epithelial cells mount an early
534 response to mycobacterial infection. *Front Cell Infect Microbiol,* 13**,** 1253037.

535 BENAM, K. H., DAUTH, S., HASSELL, B., HERLAND, A., JAIN, A., JANG, K. J., KARALIS, K.,
536 KIM, H. J., MACQUEEN, L., MAHMOODIAN, R., MUSAH, S., TORISAWA, Y. S., VAN DER
537 MEER, A. D., VILLENAVE, R., YADID, M., PARKER, K. K. & INGBER, D. E. 2015.
538 Engineered in vitro disease models. *Annu Rev Pathol,* 10**,** 195-262.

539 BENAM, K. H., VILLENAVE, R., LUCCHESI, C., VARONE, A., HUBEAU, C., LEE, H. H.,
540 ALVES, S. E., SALMON, M., FERRANTE, T. C., WEAVER, J. C., BAHINSKI, A., HAMILTON,
541 G. A. & INGBER, D. E. 2016. Small airway-on-a-chip enables analysis of human lung
542 inflammation and drug responses in vitro. *Nat Methods,* 13**,** 151-7.

543 BERRY, M. P., GRAHAM, C. M., MCNAB, F. W., XU, Z., BLOCH, S. A., ONI, T., WILKINSON, K.
544 A., BANCHEREAU, R., SKINNER, J., WILKINSON, R. J., QUINN, C., BLANKENSHIP, D.,
545 DHAWAN, R., CUSH, J. J., MEJIAS, A., RAMILO, O., KON, O. M., PASCUAL, V.,
546 BANCHEREAU, J., CHAUSSABEL, D. & O'GARRA, A. 2010. An interferon-inducible
547 neutrophil-driven blood transcriptional signature in human tuberculosis. *Nature,* 466**,** 973-7.

548 BETHENCOURT, M. A., NGUYEN, A. D. & FERRER, G. 2024. Lung Nontuberculous
549 Mycobacterial Infections. *StatPearls.* Treasure Island (FL).

550 BOHRER, A. C., CASTRO, E., HU, Z., QUEIROZ, A. T. L., TOCHENY, C. E., ASSMANN, M.,
551 SAKAI, S., NELSON, C., BAKER, P. J., MA, H., WANG, L., ZILU, W., DU BRUYN, E., RIOU,
552 C., KAUFFMAN, K. D., TUBERCULOSIS IMAGING, P., MOORE, I. N., DEL NONNO, F.,
553 PETRONE, L., GOLETTI, D., MARTINEAU, A. R., LOWE, D. M., CRONAN, M. R.,
554 WILKINSON, R. J., BARRY, C. E., VIA, L. E., BARBER, D. L., KLION, A. D., ANDRADE, B.
555 B., SONG, Y., WONG, K. W. & MAYER-BARBER, K. D. 2021. Eosinophils are part of the
556 granulocyte response in tuberculosis and promote host resistance in mice. *J Exp Med,* 218.

557 CAMPBELL, G. R. & SPECTOR, S. A. 2012. Vitamin D inhibits human immunodeficiency virus
558 type 1 and Mycobacterium tuberculosis infection in macrophages through the induction of
559 autophagy. *PLoS Pathog,* 8**,** e1002689.

560 CAVERLY, L. J., CACERES, S. M., FRATELLI, C., HAPPOLDT, C., KIDWELL, K. M.,
561 MALCOLM, K. C., NICK, J. A. & NICHOLS, D. P. 2015. Mycobacterium abscessus
562 morphotype comparison in a murine model. *PLoS One,* 10**,** e0117657.

563 CHAN, E. D., BAI, X., ORDWAY, D. J. & VERMA, D. 2016. Animal Models of Non-Tuberculous
564 Mycobacterial Infections. *Mycobacterial Diseases,* 6.

565 COWMAN, S. A., JACOB, J., HANSELL, D. M., KELLEHER, P., WILSON, R., COOKSON, W.
566 O. C., MOFFATT, M. F. & LOEBINGER, M. R. 2018. Whole-Blood Gene Expression in
567 Pulmonary Nontuberculous Mycobacterial Infection. *Am J Respir Cell Mol Biol,* 58**,** 510-518.

568 CRISTANCHO-ROJAS, C., VARLEY, C. D., LARA, S. C., KHERABI, Y., HENKLE, E. &
569 WINTHROP, K. L. 2023. Epidemiology of Mycobacterium abscessus. *Clin Microbiol Infect*.

570 DE GROOTE, M. A., JOHNSON, L., PODELL, B., BROOKS, E., BASARABA, R. & GONZALEZ-
571 JUARRERO, M. 2014. GM-CSF knockout mice for preclinical testing of agents with
572 antimicrobial activity against Mycobacterium abscessus. *J Antimicrob Chemother,* 69**,** 1057-
573 64.

574 DEINHARDT-EMMER, S., RENNERT, K., SCHICKE, E., CSERESNYES, Z., WINDOLPH, M.,
575 NIETZSCHE, S., HELLER, R., SIWCZAK, F., HAUPT, K. F., CARLSTEDT, S., SCHACKE, M.,
576 FIGGE, M. T., EHRHARDT, C., LOFFLER, B. & MOSIG, A. S. 2020. Co-infection with
577 Staphylococcus aureus after primary influenza virus infection leads to damage of the
578 endothelium in a human alveolus-on-a-chip model. *Biofabrication,* 12**,** 025012.

579 DONOHUE, M. J. 2021. Epidemiological risk factors and the geographical distribution of eight
580 Mycobacterium species. *BMC Infect Dis,* 21**,** 258.

581 FRANCO, L. H., NAIR, V. R., SCHARN, C. R., XAVIER, R. J., TORREALBA, J. R., SHILOH, M.
582 U. & LEVINE, B. 2017. The Ubiquitin Ligase Smurf1 Functions in Selective Autophagy of

583 Mycobacterium tuberculosis and Anti-tuberculous Host Defense. *Cell Host Microbe,* 21**,** 59-
584 72.

585 FU, Y. L. & HARRISON, R. E. 2021. Microbial Phagocytic Receptors and Their Potential
586 Involvement in Cytokine Induction in Macrophages. *Front Immunol,* 12**,** 662063.

587 GANGADHARAM, P. R. 1995. Beige mouse model for Mycobacterium avium complex disease.
588 *Antimicrob Agents Chemother,* 39**,** 1647-54.

589 GE, S. X., SON, E. W. & YAO, R. 2018. iDEP: an integrated web application for differential
590 expression and pathway analysis of RNA-Seq data. *BMC Bioinformatics,* 19**,** 534.

591 GONZALEZ-PEREZ, M., MARINO-RAMIREZ, L., PARRA-LOPEZ, C. A., MURCIA, M. I.,
592 MARQUINA, B., MATA-ESPINOZA, D., RODRIGUEZ-MIGUEZ, Y., BAAY-GUZMAN, G. J.,
593 HUERTA-YEPEZ, S. & HERNANDEZ-PANDO, R. 2013. Virulence and immune response
594 induced by Mycobacterium avium complex strains in a model of progressive pulmonary
595 tuberculosis and subcutaneous infection in BALB/c mice. *Infect Immun,* 81**,** 4001-12.

596 HOANG, T. N. M., CSERESNYES, Z., HARTUNG, S., BLICKENSDORF, M., SAFFER, C.,
597 RENNERT, K., MOSIG, A. S., VON LILIENFELD-TOAL, M. & FIGGE, M. T. 2022. Invasive
598 aspergillosis-on-chip: A quantitative treatment study of human Aspergillus fumigatus infection.
599 *Biomaterials,* 283**,** 121420.

600 HUH, D., LESLIE, D. C., MATTHEWS, B. D., FRASER, J. P., JUREK, S., HAMILTON, G. A.,
601 THORNELOE, K. S., MCALEXANDER, M. A. & INGBER, D. E. 2012a. A human disease
602 model of drug toxicity-induced pulmonary edema in a lung-on-a-chip microdevice. *Sci Transl*
603 *Med,* 4**,** 159ra147.

604 HUH, D., MATTHEWS, B. D., MAMMOTO, A., MONTOYA-ZAVALA, M., HSIN, H. Y. & INGBER,
605 D. E. 2010. Reconstituting organ-level lung functions on a chip. *Science,* 328**,** 1662-8.

606 HUH, D., TORISAWA, Y. S., HAMILTON, G. A., KIM, H. J. & INGBER, D. E. 2012b.
607 Microengineered physiological biomimicry: organs-on-chips. *Lab Chip,* 12**,** 2156-64.

608 IAKOBACHVILI, N., LEON-ICAZA, S. A., KNOOPS, K., SACHS, N., MAZERES, S., SIMEONE,
609 R., PEIXOTO, A., BERNARD, C., MURRIS-ESPIN, M., MAZIERES, J., CAM, K., CHALUT,
610 C., GUILHOT, C., LOPEZ-IGLESIAS, C., RAVELLI, R. B. G., NEYROLLES, O., MEUNIER,
611 E., LUGO-VILLARINO, G., CLEVERS, H., COUGOULE, C. & PETERS, P. J. 2022.
612 Mycobacteria-host interactions in human bronchiolar airway organoids. *Mol Microbiol,* 117**,**
613 682-692.

614 JAIN, A., BARRILE, R., VAN DER MEER, A. D., MAMMOTO, A., MAMMOTO, T., DE
615 CEUNYNCK, K., AISIKU, O., OTIENO, M. A., LOUDEN, C. S., HAMILTON, G. A.,
616 FLAUMENHAFT, R. & INGBER, D. E. 2018. Primary Human Lung Alveolus-on-a-chip Model
617 of Intravascular Thrombosis for Assessment of Therapeutics. *Clin Pharmacol Ther,* 103**,** 332-
618 340.

619 JOHANSEN, M. D. & KREMER, L. 2020. CFTR Depletion Confers Hypersusceptibility to
620 Mycobacterium fortuitum in a Zebrafish Model. *Front Cell Infect Microbiol,* 10**,** 357.

621 KILINC, G., WALBURG, K. V., FRANKEN, K., VALKENBURG, M. L., AUBRY, A., HAKS, M. C.,
622 SARIS, A. & OTTENHOFF, T. H. M. 2022. Development of Human Cell-Based In Vitro
623 Infection Models to Determine the Intracellular Survival of Mycobacterium avium. *Front Cell*
624 *Infect Microbiol,* 12**,** 872361.

625 KIM, S. R., YU, J. Y., KIM, S. Y., KIM, D. H. & JHUN, B. W. 2023. Clinical Characteristics and
626 Treatment Outcomes of Mycobacterium fortuitum Pulmonary Disease. *Microbiol Spectr,* 11**,**
627 e0205123.

628 KIM, S. Y., CHOI, J. A., CHOI, S., KIM, K. K., SONG, C. H. & KIM, E. M. 2024. Advances in an
629 In Vitro Tuberculosis Infection Model Using Human Lung Organoids for Host-Directed
630 Therapies. *PLoS Pathog,* 20**,** e1012295.

631 KIMMEY, J. M., HUYNH, J. P., WEISS, L. A., PARK, S., KAMBAL, A., DEBNATH, J., VIRGIN, H.
632 W. & STALLINGS, C. L. 2015. Unique role for ATG5 in neutrophil-mediated immunopathology
633 during M. tuberculosis infection. *Nature,* 528**,** 565-9.

634 KLEVER, A. M., ALEXANDER, K. A., ALMEIDA, D., ANDERSON, M. Z., BALL, R. L., BEAMER,
635 G., BOGGIATTO, P., BUIKSTRA, J. E., CHANDLER, B., CLAEYS, T. A., CONCHA, A. E.,
636 CONVERSE, P. J., DERBYSHIRE, K. M., DOBOS, K. M., DUPNIK, K. M., ENDSLEY, J. J.,
637 ENDSLEY, M. A., FENNELLY, K., FRANCO-PAREDES, C., HAGGE, D. A., HALL-
638 STOODLEY, L., HAYES, D., JR., HIRSCHFELD, K., HOFMAN, C. A., HONDA, J. R., HULL,
639 N. M., KRAMNIK, I., LACOURCIERE, K., LAHIRI, R., LAMONT, E. A., LARSEN, M. H.,
640 LEMAIRE, T., LESELLIER, S., LEE, N. R., LOWRY, C. A., MAHFOOZ, N. S., MCMICHAEL,
641 T. M., MERLING, M. R., MILLER, M. A., NAGAJYOTHI, J. F., NELSON, E.,
642 NUERMBERGER, E. L., PENA, M. T., PEREA, C., PODELL, B. K., PYLE, C. J., QUINN, F.
643 D., RAJARAM, M. V. S., MEJIA, O. R., ROTHOFF, M., SAGO, S. A., SALVADOR, L. C. M.,
644 SIMONSON, A. W., SPENCER, J. S., SREEVATSAN, S., SUBBIAN, S., SUNSTRUM, J.,
645 TOBIN, D. M., VIJAYAN, K. K. V., WRIGHT, C. T. O. & ROBINSON, R. T. 2023. The Many
646 Hosts of Mycobacteria 9 (MHM9): A conference report. *Tuberculosis (Edinb),* 142**,** 102377.

647 KREMER, M. D. J. A. L. 2020. CFTR Depletion Confers Hypersusceptibility to Mycobacterium
648 fortuitum in a Zebrafish Model. *Frontiers in Cellular and Infection Microbiology,* 10.

649 LAGUNE, M., KREMER, L. & HERRMANN, J. L. 2023. Mycobacterium abscessus, a complex of
650 three fast-growing subspecies sharing virulence traits with slow-growing mycobacteria. *Clin*
651 *Microbiol Infect*.

652 LEON-ICAZA, S. A., BAGAYOKO, S., VERGE, R., IAKOBACHVILI, N., FERRAND, C.,
653 AYDOGAN, T., BERNARD, C., SANCHEZ DAFUN, A., MURRIS-ESPIN, M., MAZIERES, J.,
654 BORDIGNON, P. J., MAZERES, S., BERNES-LASSERRE, P., RAME, V., LAGARDE, J. M.,
655 MARCOUX, J., BOUSQUET, M. P., CHALUT, C., GUILHOT, C., CLEVERS, H., PETERS, P.
656 J., MOLLE, V., LUGO-VILLARINO, G., CAM, K., BERRY, L., MEUNIER, E. & COUGOULE,
657 C. 2023. Druggable redox pathways against Mycobacterium abscessus in cystic fibrosis
658 patient-derived airway organoids. *PLoS Pathog,* 19**,** e1011559.

659 LI, J., WANG, Z., CHU, Q., JIANG, K., LI, J. & TANG, N. 2018. The Strength of Mechanical
660 Forces Determines the Differentiation of Alveolar Epithelial Cells. *Dev Cell,* 44**,** 297-312 e5.

661 LI, J., WEN, A. M., POTLA, R., BENSHIRIM, E., SEEBARRAN, A., BENZ, M. A., HENRY, O. Y.
662 F., MATTHEWS, B. D., PRANTIL-BAUN, R., GILPIN, S. E., LEVY, O. & INGBER, D. E. 2019.
663 AAV-mediated gene therapy targeting TRPV4 mechanotransduction for inhibition of
664 pulmonary vascular leakage. *APL Bioeng,* 3**,** 046103.

665 LINDESTAM ARLEHAMN, C. S., BENSON, B., KUAN, R., DILL-MCFARLAND, K. A.,
666 PETERSON, G. J., PAUL, S., NGUYEN, F. K., GILMAN, R. H., SAITO, M., TAPLITZ, R.,
667 ARENTZ, M., GOSS, C. H., AITKEN, M. L., HORNE, D. J., SHAH, J. A., SETTE, A. & HAWN,
668 T. R. 2022. T-cell deficiency and hyperinflammatory monocyte responses associate with
669 Mycobacterium avium complex lung disease. *Front Immunol,* 13**,** 1016038.

670 LUKE, C. J., MARKOVINA, S., GOOD, M., WIGHT, I. E., THOMAS, B. J., LINNEMAN, J. M.,
671 LANIK, W. E., KOROLEVA, O., COFFMAN, M. R., MIEDEL, M. T., GONG, Q., ANDRESS, A.,
672 CAMPOS GUERRERO, M., WANG, S., CHEN, L., BEATTY, W. L., HAUSMANN, K. N.,
673 WHITE, F. V., FITZPATRICK, J. A. J., ORVEDAHL, A., PAK, S. C. & SILVERMAN, G. A.
674 2022. Lysoptosis is an evolutionarily conserved cell death pathway moderated by intracellular
675 serpins. *Commun Biol,* 5**,** 47.

676 MERCALDO, R. A., MARSHALL, J. E., CANGELOSI, G. A., DONOHUE, M., FALKINHAM, J.
677 O., 3RD, FIERER, N., FRENCH, J. P., GEBERT, M. J., HONDA, J. R., LIPNER, E. M.,
678 MARRAS, T. K., MORIMOTO, K., SALFINGER, M., STOUT, J., THOMSON, R. & PREVOTS,
679 D. R. 2023. Environmental risk of nontuberculous mycobacterial infection: Strategies for
680 advancing methodology. *Tuberculosis (Edinb),* 139**,** 102305.

681 MISHRA, R., HANNEBELLE, M., PATIL, V. P., DUBOIS, A., GARCIA-MOUTON, C., KIRSCH, G.
682 M., JAN, M., SHARMA, K., GUEX, N., SORDET-DESSIMOZ, J., PEREZ-GIL, J., PRAKASH,
683 M., KNOTT, G. W., DHAR, N., MCKINNEY, J. D. & THACKER, V. V. 2023.
684 Mechanopathology of biofilm-like Mycobacterium tuberculosis cords. *Cell,* 186**,** 5135-5150
685 e28.

686 NOBS, E., LASCHANZKY, K., MUNKE, K., MOVERT, E., VALFRIDSSON, C. & CARLSSON, F.
687 2024. Cytosolic serpins act in a cytoprotective feedback loop that limits ESX-1-dependent
688 death of Mycobacterium marinum-infected macrophages. *mBio*, e0038424.

689 ORDWAY, D., HENAO-TAMAYO, M., SMITH, E., SHANLEY, C., HARTON, M., TROUDT, J.,
690 BAI, X., BASARABA, R. J., ORME, I. M. & CHAN, E. D. 2008. Animal model of
691 Mycobacterium abscessus lung infection. *J Leukoc Biol,* 83, 1502-11.

692 ORME, I. M. & ORDWAY, D. J. 2014. Host response to nontuberculous mycobacterial infections
693 of current clinical importance. *Infect Immun,* 82, 3516-22.

694 QIN, M. H., MADIRAJU, M. V. & RAJAGOPALAN, M. 1999. Characterization of the functional
695 replication origin of Mycobacterium tuberculosis. *Gene,* 233, 121-30.

696 RAMPACCI, E., STEFANETTI, V., PASSAMONTI, F. & HENAO-TAMAYO, M. 2020. Preclinical
697 Models of Nontuberculous Mycobacteria Infection for Early Drug Discovery and Vaccine
698 Research. *Pathogens,* 9.

699 ROQUET-BANERES, F., ALCARAZ, M., HAMELA, C., ABENDROTH, J., EDWARDS, T. E. &
700 KREMER, L. 2023. In Vitro and In Vivo Efficacy of NITD-916 against Mycobacterium
701 fortuitum. *Antimicrob Agents Chemother,* 67, e0160722.

702 TABONE, O., VERMA, R., SINGHANIA, A., CHAKRAVARTY, P., BRANCHETT, W. J., GRAHAM,
703 C. M., LEE, J., TRANG, T., REYNIER, F., LEISSNER, P., KAISER, K., RODRIGUE, M.,
704 WOLTMANN, G., HALDAR, P. & O'GARRA, A. 2021. Blood transcriptomics reveal the
705 evolution and resolution of the immune response in tuberculosis. *J Exp Med,* 218.

706 THACKER, V. V., DHAR, N., SHARMA, K., BARRILE, R., KARALIS, K. & MCKINNEY, J. D.
707 2020. A lung-on-chip model of early Mycobacterium tuberculosis infection reveals an
708 essential role for alveolar epithelial cells in controlling bacterial growth. *Elife,* 9.

709 TOURE, H., GALINDO, L. A., LAGUNE, M., GLATIGNY, S., WATERHOUSE, R. M., GUENAL, I.,
710 HERRMANN, J. L., GIRARD-MISGUICH, F. & SZUPLEWSKI, S. 2023. Mycobacterium
711 abscessus resists the innate cellular response by surviving cell lysis of infected phagocytes.
712 *PLoS Pathog,* 19, e1011257.

713 VARLEY, C. D. & WINTHROP, K. L. 2022. Nontuberculous Mycobacteria: Diagnosis and
714 Therapy. *Clin Chest Med,* 43, 89-98.

715 WANG, L., MA, H., WEN, Z., NIU, L., CHEN, X., LIU, H., ZHANG, S., XU, J., ZHU, Y., LI, H.,
716 CHEN, H., SHI, L., WAN, L., LI, L., LI, M., WONG, K. W. & SONG, Y. 2023a. Single-cell RNA-

717 sequencing reveals heterogeneity and intercellular crosstalk in human tuberculosis lung. *J*
718 *Infect,* 87**,** 373-384.

719 WANG, L., ZHENG, X., MA, J., GU, J. & SHA, W. 2023b. Comparative Proteomic Analysis of
720 Exosomes Derived from Patients Infected with Non-Tuberculous Mycobacterium and
721 Mycobacterium tuberculosis. *Microorganisms,* 11.

722 WANG, P., YANG, G. L., HE, Y. F., SHEN, Y. H., HAO, X. H., LIU, H. P., SHEN, H. B., WANG, L.
723 & SHA, W. 2024. Single-cell transcriptomics of blood identified IFIT1(+) neutrophil subcluster
724 expansion in NTM-PD patients. *Int Immunopharmacol,* 137**,** 112412.

725 WINTHROP, K. L., MARRAS, T. K., ADJEMIAN, J., ZHANG, H., WANG, P. & ZHANG, Q. 2020.
726 Incidence and Prevalence of Nontuberculous Mycobacterial Lung Disease in a Large U.S.
727 Managed Care Health Plan, 2008-2015. *Ann Am Thorac Soc,* 17**,** 178-185.

728

729 **Figure legends**

730 **Figure 1**. **Establishment of a fully humanized alveolus lung-on-a-chip (ALoC) model system**
731 **A.** Schematic of a human alveolus and the surrounding vasculature, highlighting alveolar epithelial
732 type I (ATI), alveolar epithelial type II (AT2) cells, and alveolar macrophages in the alveolar sac,
733 with pulmonary microvascular endothelial cells lining the vasculature. **B.** Schematic of the ALoC
734 model for *M. fortuitum* infection. The apical channel contains primary human alveolar epithelial
735 cells (ATI and ATII) with or without human $CD14^+$ peripheral blood-derived macrophages, while
736 the basal channel is lined by human primary pulmonary microvascular endothelial cells
737 (HMVECs). **C.** Stitched image of the apical channel of the ALoC at 15 days of culture highlighting
738 AT1 cells ($HT1^+$, magenta) and AT2 cells ($HT2^+$, green). Nuclei are labelled with DAPI (blue).
739 Scale bar = 100 μm. **D (left).** Epifluorescent image of differentiated AT1 and AT2 cells on the
740 ALoC. Scale bar = 50 μm. **D (right).** Three-dimensional immunofluorescence reconstruction of
741 ALoC after 15 days of culture, highlighting differentiated AT2 cells and AT1 cells. Scale bar = 100
742 μm**. E.** Cross-sectional image of the ALoC highlighting AT1 and AT2 cells in a monolayer. Scale
743 bar = 50 μm**.** Images are representative of at least 3 independent chips from 2 independent
744 experiments.

745 **Figure 2. Human macrophages reside on the alveolar surface in the humanized ALoC A.**
746 Schematic of the addition of macrophages to the apical channel. **B.** Stitched image of the apical
747 epithelial channel of the ALoC after the addition of macrophages ($CD14^+$, orange) on the ALoC.
748 Nuclei are labelled with DAPI. Scale bar = 100 μm**. C.** Epifluorescent image of differentiated
749 macrophages dispersed amongst AT1 and AT2 cells on the ALoC. Scale bar = 50 μm. **D (left).**
750 Cross-sectional image of the ALoC showing AT1 cells ($HT1^+$, magenta), AT2 cells ($HT2^+$, green),
751 and macrophages ($CD14^+$, orange). Scale bar = 50 μm**. D (right).** Three-dimensional
752 reconstruction of ALoC highlighting the addition of macrophages on the surface of differentiated
753 AT1 and AT2 cells. Scale bar = 50 μm**.** Images are representative of at least 3 independent chips

754 from 2 independent experiments. **E.** Cross-sectional image of the ALoC with macrophages
755 highlighting macrophages laying on the surface of AT1 and AT2 cells. Scale bar = 50 μm**.** Images
756 are representative of at least 3 independent chips from 2 independent experiments.

757 **Figure 3. *Mycobacterium fortuitum* infection on an Alveolus Lung-on-a-Chip without**
758 **macrophages A.** Schematic of *M. fortuitum* addition to the ALoC. mCherry-expressing *M.*
759 *fortuitum* was added to the ALoC at an MOI of 1 with respect to the alveolar epithelial cells. After
760 1 hour of static incubation at 37°C, ALoCs were washed and returned to ALI. **B.** Epifluorescent
761 image *M. fortuitum* (mCherry, white)-infected AT1 (HT1+, magenta) and AT2 (HT2+, green) cells.
762 Scale bar = 50 μm. **C (left).** Cross-sectional image of *M. fortuitum* (mCherry, white) infection on
763 ALoC with AT1 and AT2 cells. Scale bar = 50 μm**. C (right).** Three-dimensional reconstruction of
764 an infected ALoC without macrophages. Scale bar = 50 μm**. D.** A single z-slice image of an
765 uninfected ALoC without macrophages containing AT1, AT2 and AT1/AT2-positive cells, with
766 AT1/AT2 cells highlighted by asterisks. Nuclei are labelled with DAPI (blue). Scale bar = 30 μm.
767 **E.** Pie chart representing the ratio of AT1, AT2 or AT1/AT2-positive cells on ALoCs without
768 macrophages. Cells were counted from 3 independent uninfected ALoCs without macrophages
769 (number of cells counted per chip range from 900-1300 total cells) and averaged. **F.** A single z-
770 slice image of an infected ALoC without macrophages containing AT1, AT2 and AT1/AT2-positive
771 cells, with AT1/AT2 cells highlighted by asterisks. Nuclei are labelled with DAPI (blue).Scale bar
772 = 30 μm. **G.** Pie chart representing the ratio of AT1, AT2 or AT1/AT2-positive cells on *M. fortuitum*-
773 infected ALoCs without macrophages. Cells were counted from 3 independent infected ALoCs
774 without macrophages (number of cells counted per chip range from 800-900 total cells) and
775 averaged. Images are representative of at least 3 independent chips from 2 independent
776 experiments.

777 **Figure 4**. ***Mycobacterium fortuitum* infection on an Alveolus Lung-on-a-Chip containing**
778 **macrophages A.** Schematic of *M. fortuitum* infection on ALoC containing macrophages. 24 hours

779 after the addition macrophages, *M. fortuitum* was added to the ALoC at an MOI of 1 with respect
780 to the alveolar epithelial cells, incubated at 37°C for 1 hour, washed, and returned to ALI. **B**.
781 Epifluorescent image of an *M.fortuitum* (mCherry, white)-infected ALoC with macrophages
782 containing AT1 cells (HT1+, magenta) and macrophages (CD14+, orange). Scale bar = 20 μm.
783 **C.** Epifluorescent image of an *M.fortuitum* (mCherry, white)-infected ALoC with macrophages
784 containing AT2 cells (HT2+, green) and macrophages (CD14+, orange). Scale bar = 20 μm. **D**
785 **(left).** Cross-sectional image of *M. fortuitum* infection on ALoC with the addition of macrophages,
786 highlighting intracellular M. fortuitum bacilli within macrophages (CD14+, orange) rather than AT2
787 (HT2+, green) cells. Scale bar = 50 μm. **D (right).** Three-dimensional reconstructed image of an
788 ALoC with macrophages containing AT2 cells and *M.fortuitum*-infected macrophages. Scale bar
789 = 100 μm. **E.** Quantification of *M. fortuitum* bacilli found intracellularly within macrophages or AT1
790 cells. Each point represents the cumulative number of *M. fortuitum* bacilli counted in each cell
791 type for 10 fields within a single chip (N=3 independent chips, $p<0.0001$ by unpaired Student's t-
792 test). **F.** Quantification of *M. fortuitum* bacilli found intracellularly within macrophages or AT2 cells.
793 Each point represents the cumulative number of *M. fortuitum* bacilli counted in each cell type for
794 10 fields within a single chip (N=3 independent chips, $p<0.0001$ by unpaired Student's t-test).
795 Images are representative of at least 3 independent chips from three independent experiments.

796 **Figure 5**. **Bulk RNA-seq Analysis of *M. fortuitum*-infected ALoCs with macrophages A.**
797 Heat-map of the top 2000 genes expressed in uninfected and *M. fortuitum*-infected ALoCs (24
798 hours post-infection) (N=3 per group) using Pearson distance and average linkage. **B.** The $-\log_{10}$
799 (Adjusted p-Value) was plotted against $\log_2$ fold change to create a volcano plot representing the
800 top 25 differentially expressed genes (DEGs). Genes with an adjusted p-value<25 and $\log_2$ fold
801 change<2 were filtered from this analysis. **C.** Heat map comparing the $\log_2$ fold change of the
802 most differentially expressed chemokines and cytokines in ALoCs infected with *M. fortuitum*
803 versus uninfected ALoCs after 24 hours of infection. **D.** Heat map comparing the $\log_2$ fold change

804 of the most differentially expressed SERPINs in ALoCS infected with *M. fortuitum* versus
805 uninfected ALoCs after 24 hours of infection.

806 **Supplemental Figure Legends**

807 **Supplemental Figure 1**. **Establishment of the Alveolus Lung-on-a-Chip Model**. **A.** Typical
808 timeline of a single alveolus lung-on-a-chip (ALoC) experiment. **B.** Stitched image of the entire
809 apical channel containing AT1 (HT1+, magenta) and AT2 cells (HT2+, green). Nuclei are labelled
810 with DAPI (blue). Scale bar = 500 µm. **C.** A single z-slice image highlighting KRT5+ cells (orange)
811 on an uninfected ALoC. Nuclei are labelled with DAPI (blue). Scale bar = 50 µm. **D.** A single z-
812 slice image of the bottom of the basal compartment of an uninfected ALoC containing
813 macrophages. Human lung microvascular endothelial cells (HMVEC) are labelled with VE-
814 cadherin (magenta). Nuclei are labelled with DAPI. Scale bar = 50 µm. **E.** Stitched image of the
815 entire apical channel of an ALoC containing macrophages (CD14+, orange), AT1 cells (HT1+,
816 magenta), and AT2 cells (HT2+, green). Nuclei are labelled DAPI (blue). Scale bar = 500 µm. **F.**
817 Brightfield image of an uninfected ALoC immediately after the addition human $CD14^+$ peripheral
818 blood-derived macrophages (macrophages) on top of the alveolar epithelial cells **(left)**. Brightfield
819 image of an uninfected ALoC 24 hours after the addition of macrophages (**right)**.

820 **Supplemental Figure 2**. **Bulk RNA-sequencing analysis of *M. fortuitum*-infected ALoCs A.**
821 Total raw read counts of uninfected (n=3) and *M. fortuitum*-infected (n=3) ALoCs. **B.** Pearson
822 (average linkage) clustering of *M. fortuitum*-infected ALoCs and uninfected ALoCs.

Figure 1

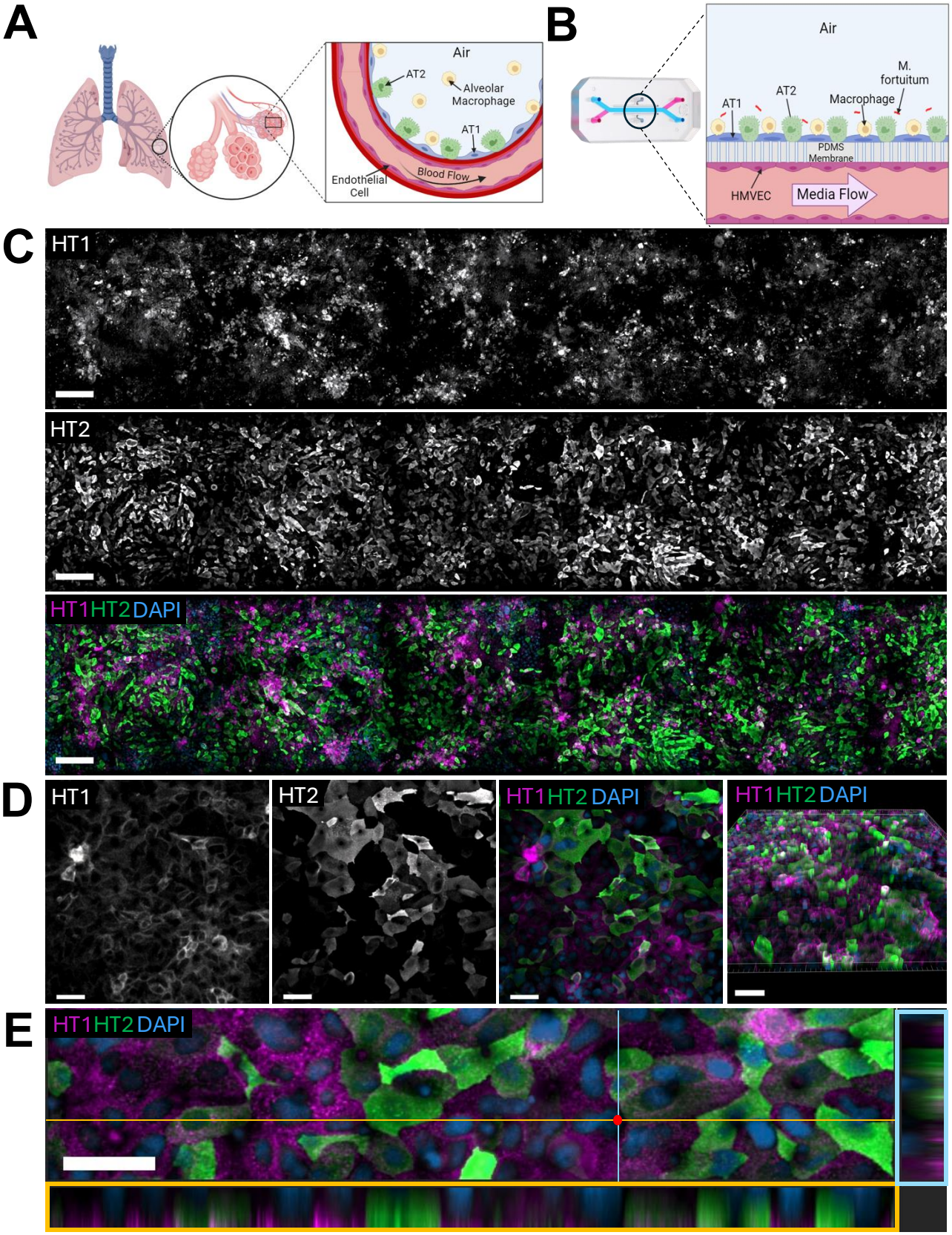
A
Air
AT2
Alveolar Macrophage
AT1
Endothelial Cell
Blood Flow
B
Air
M. fortuitum
AT1
AT2
Macrophage
PDMS Membrane
HMVEC
Media Flow
C
HT1
HT2
HT1 HT2 DAPI
D
HT1
HT2
HT1 HT2 DAPI
HT1 HT2 DAPI
E
HT1 HT2 DAPI

Figure 2

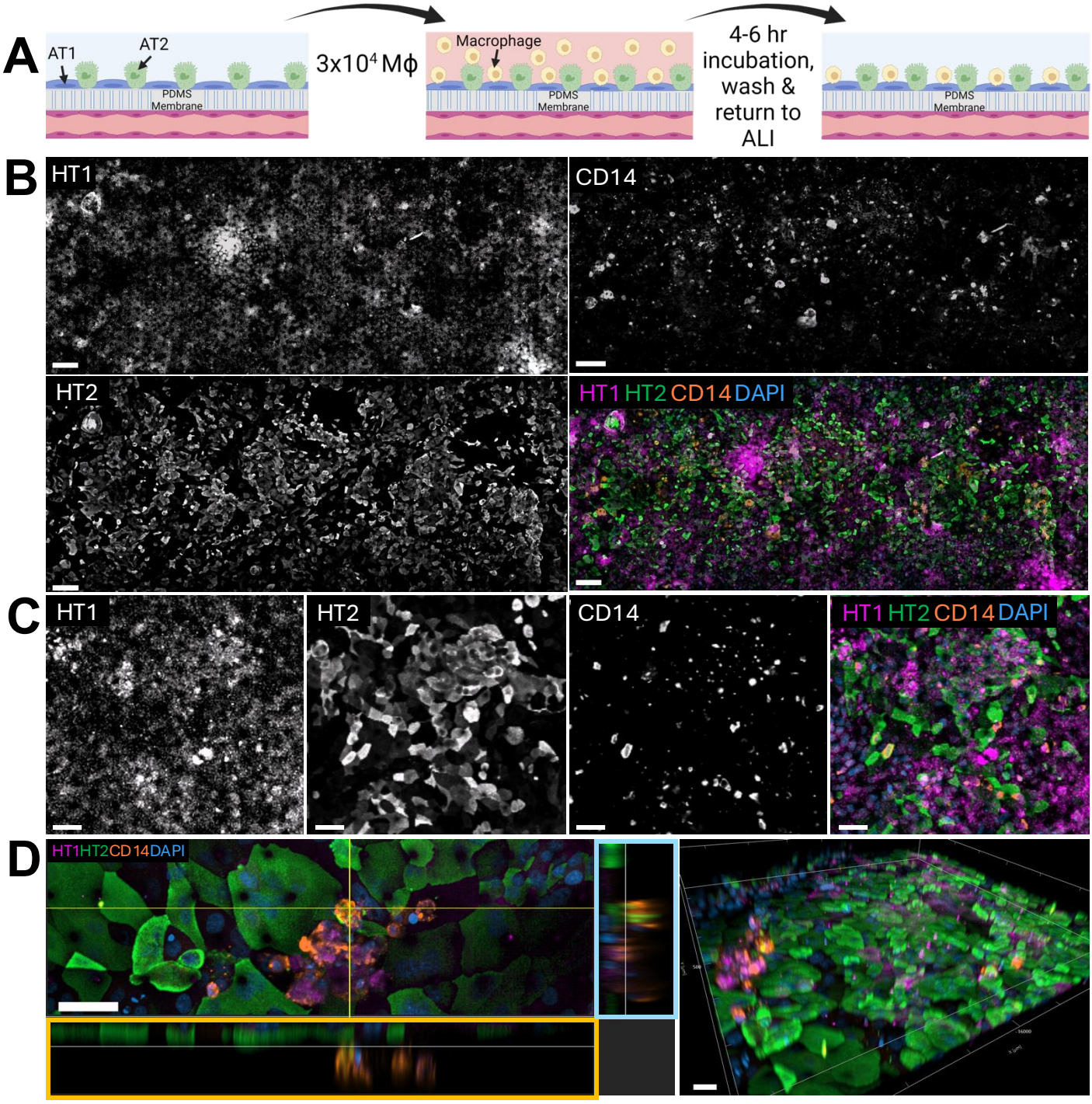
A
AT1
AT2
PDMS Membrane
3x10⁴ Mϕ
Macrophage
PDMS Membrane
4-6 hr incubation, wash & return to ALI
PDMS Membrane
B
HT1
CD14
HT2
HT1 HT2 CD14 DAPI
C
HT1
HT2
CD14
HT1 HT2 CD14 DAPI
D
HT1HT2CD14DAPI

Figure 3

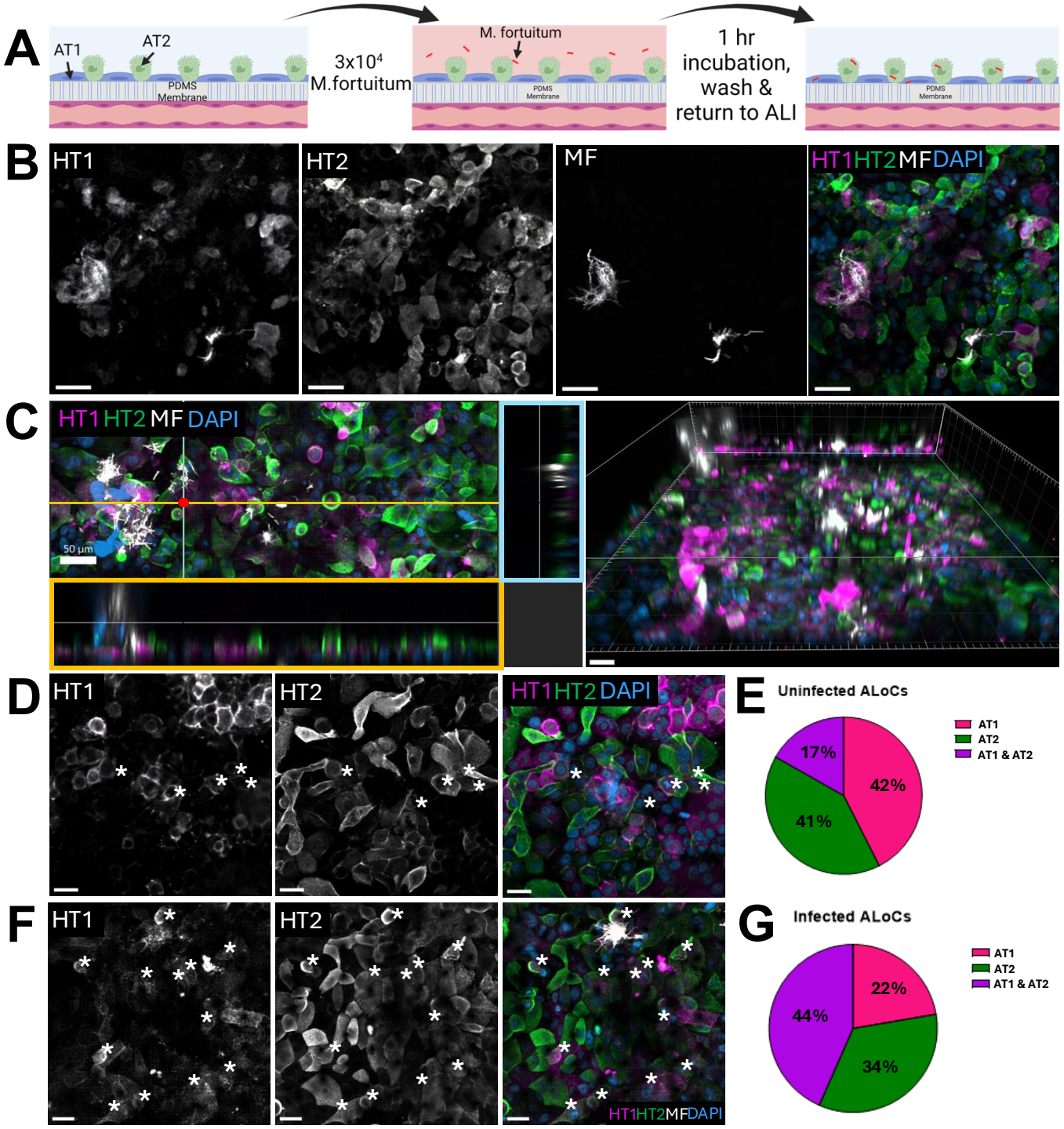
A
AT1
AT2
PDMS Membrane
3x10⁴ M.fortuitum
M. fortuitum
1 hr incubation, wash & return to ALI
B
HT1
HT2
MF
HT1HT2MFDAPI
C
HT1 HT2 MF DAPI
50 µm
D
HT1
HT2
HT1HT2DAPI
E
Uninfected ALoCs
AT1
AT2
AT1 & AT2
17%
42%
41%
F
HT1
HT2
HT1HT2MFDAPI
G
Infected ALoCs
AT1
AT2
AT1 & AT2
22%
44%
34%

Figure 4

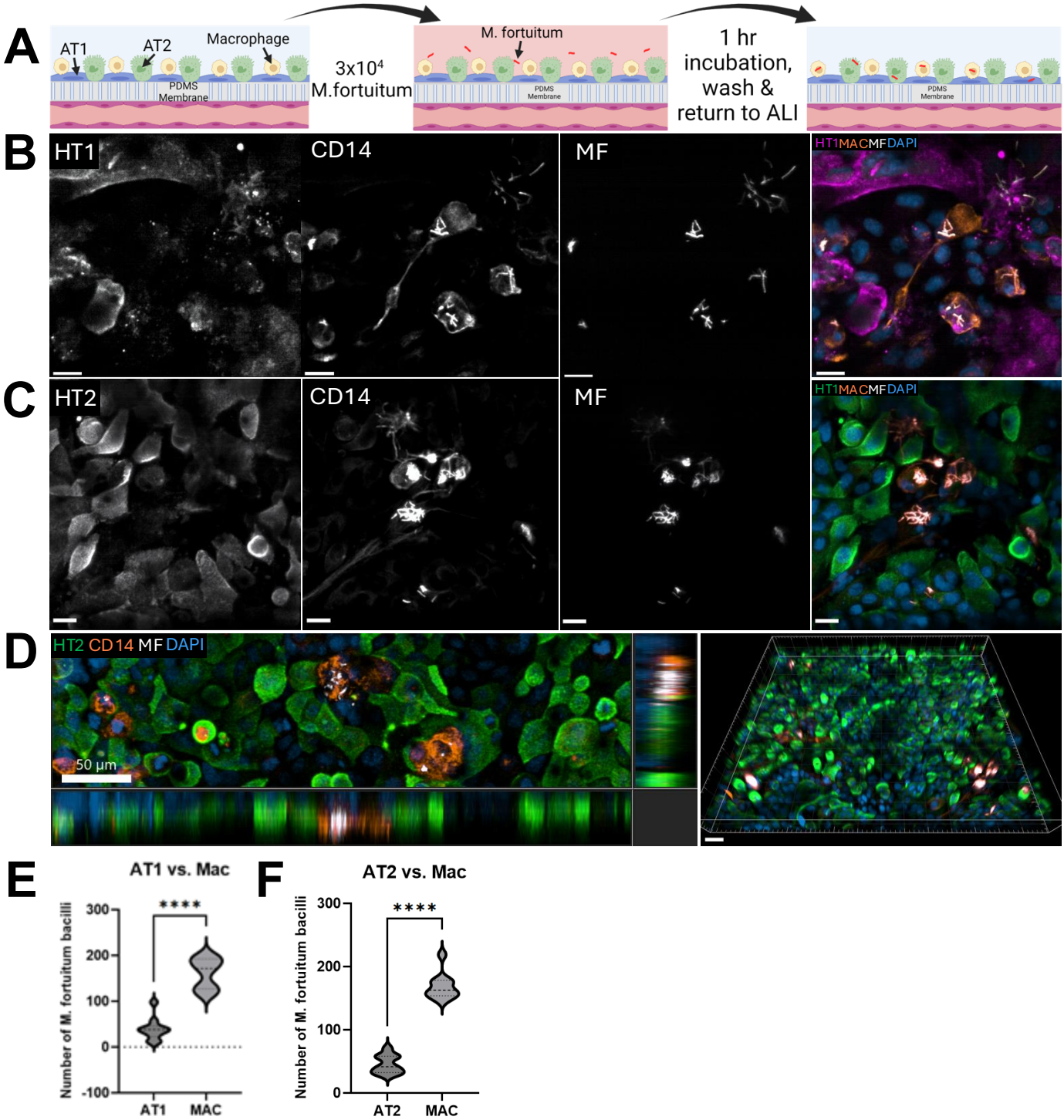
A
AT1
AT2
Macrophage
PDMS Membrane
3x10⁴ M.fortuitum
M. fortuitum
1 hr incubation, wash & return to ALI
B
HT1
CD14
MF
HT1MACMFDAPI
C
HT2
CD14
MF
HT1MACMFDAPI
D
HT2 CD14 MF DAPI
50 µm
E
AT1 vs. Mac
Number of M. fortuitum bacilli
****
AT1
MAC
F
AT2 vs. Mac
Number of M. fortuitum bacilli
****
AT2
MAC

Figure 5

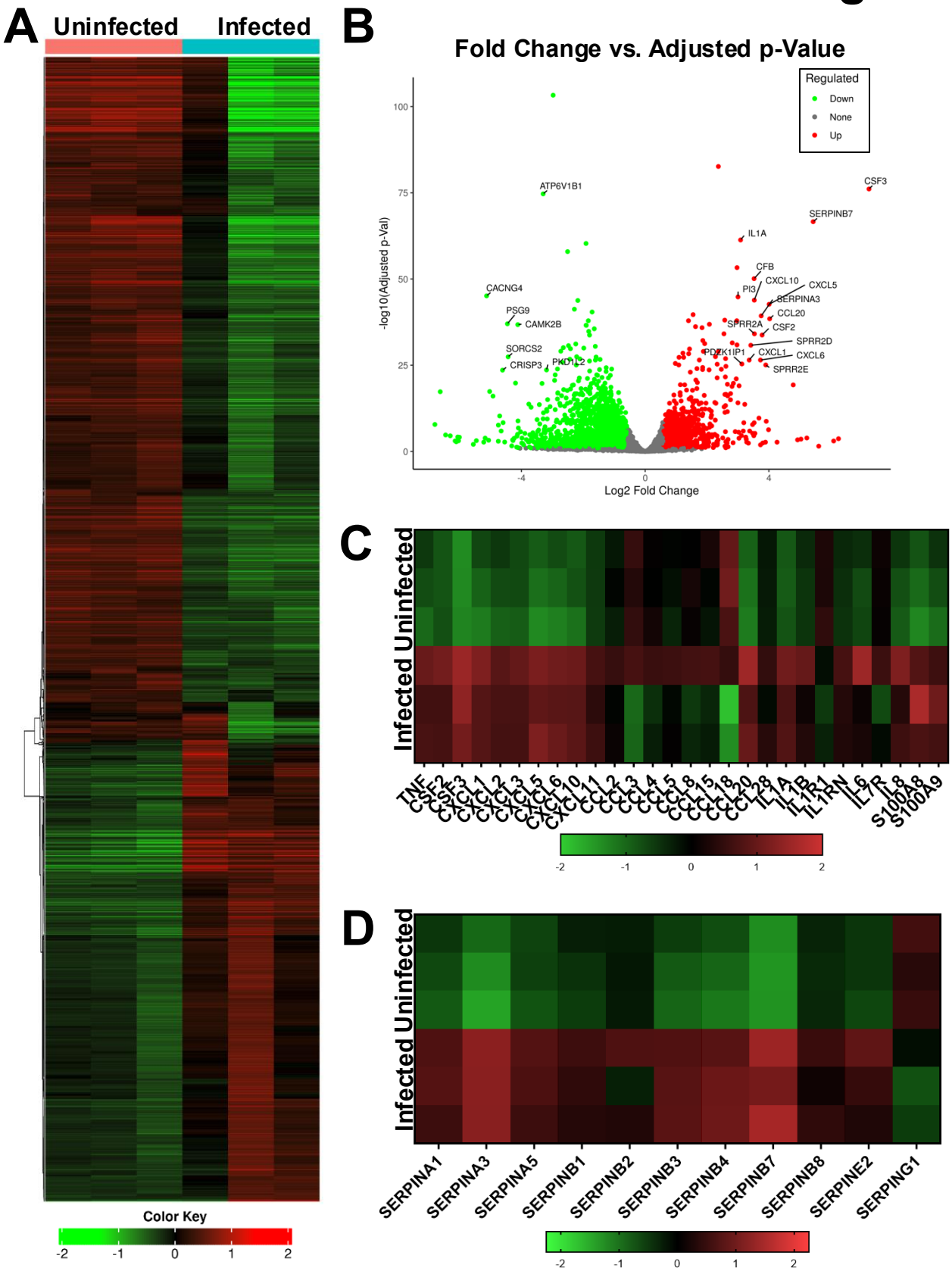
A
Uninfected
Infected
Color Key
-2
-1
0
1
2
B
Fold Change vs. Adjusted p-Value
Regulated
Down
None
Up
-log10(Adjusted p-Val)
Log2 Fold Change
ATP6V1B1
CACNG4
PSG9
CAMK2B
SORCS2
CRISP3
PKD1L2
CSF3
SERPINB7
IL1A
CFB
CXCL10
CXCL5
PI3
SERPINA3
CCL20
SPRR2A
CSF2
SPRR2D
PDZK1IP1
CXCL1
CXCL6
SPRR2E
C
Infected Uninfected
TNF
CSF2
CSF3
CXCL1
CXCL2
CXCL3
CXCL5
CXCL6
CXCL10
CXCL11
CCL2
CCL3
CCL4
CCL5
CCL8
CCL15
CCL18
CCL20
CCL28
IL1A
IL1B
IL1R1
IL1RN
IL6
IL7R
IL8
S100A8
S100A9
D
Infected Uninfected
SERPINA1
SERPINA3
SERPINA5
SERPINB1
SERPINB2
SERPINB3
SERPINB4
SERPINB7
SERPINB8
SERPINE2
SERPING1

Table 1. The most significant up-regulated and down-regulated GO Biological Process pathways from M. fortuitum-infected ALoCs containing macrophages

Direction	GO Biological Process	Statistic	Genes	adj.Pval
Up	Response to bacterium	7.3996	438	1.1e-09
	Humoral immune response	6.5518	138	6.0e-07
	Defense response to bacterium	6.3097	169	1.1e-06
	Antimicrobial humoral response	6.0602	65	1.9e-05
	Response to molecule of bacterial origin	5.5061	251	3.7e-05
	Chemotaxis	5.2453	444	8.2e-05
	Taxis	5.2402	445	8.2e-05
	Response to lipopolysaccharide	5.2654	240	8.2e-05
	Antimicrobial humoral immune response mediated by antimicrobial peptide	5.6504	41	1.4e-04
Down	MRNA processing	-6.8939	402	4.4e-08
	RNA splicing	-6.5273	385	2.3e-07
	Histone modification	-5.7112	429	1.6e-05
	Proteasome-mediated ubiquitin-dependent protein catabolic process	-5.5755	410	2.5e-05
	Proteasomal protein catabolic process	-5.534	470	2.5e-05
	Chromatin organization	-5.4523	478	3.2e-05
	NcRNA metabolic process	-5.3774	477	4.2e-05
	Peptidyl-lysine modification	-5.128	343	1.5e-04
	RNA splicing via transesterification reactions with bulged adenosine as nucleophile	-5.1146	265	1.5e-04
	MRNA splicing via spliceosome	-5.1146	265	1.5e-04
	RNA splicing via transesterification reactions	-5.097	269	1.5e-04

Table 2. The most significant up-regulated and down-regulated GO Molecular Function pathways from M. fortuitum-infected ALoCs containing macrophages

Direction	GO Molecular Function	Statistic	Genes	adj.Pval
Up	Transmembrane signaling receptor activity	8.0205	486	1.9e-12
	Receptor ligand activity	6.4443	275	6.9e-08
	Signaling receptor regulator activity	6.3634	295	6.9e-08
	Signaling receptor activator activity	6.3463	281	6.9e-08
	Cytokine activity	5.657	148	4.8e-06
	Channel activity	5.1005	274	3.6e-05
	Passive transmembrane transporter activity	5.1005	274	3.6e-05
	Glycosaminoglycan binding	5.1296	151	3.7e-05
	Ion channel activity	4.8906	248	8.2e-05
	Calcium ion binding	4.8317	497	8.2e-05
	G protein-coupled receptor activity	4.872	193	8.3e-05
	Gated channel activity	4.7825	188	1.1e-04
	Extracellular matrix structural constituent	4.7767	119	1.3e-04
	Cation channel activity	4.7291	184	1.3e-04
	Inorganic molecular entity transmembrane transporter activity	4.6534	455	1.3e-04
	Heparin binding	4.4603	110	4.5e-04
	Endopeptidase regulator activity	4.3733	123	6.1e-04
	Inorganic cation transmembrane transporter activity	4.2753	363	6.3e-04
Down	Catalytic activity acting on RNA	-5.0214	311	3.8e-04
	Histone binding	-4.8025	216	6.4e-04